

■ Metal–Organic Frameworks | *Hot Paper* |

# Exploring the Influence of Halogen Coordination Effect of Stable Bimetallic MOFs on Oxygen Evolution Reaction

Jia-Ni Lu,<sup>[a]</sup> Jiang Liu,<sup>\*,[a]</sup> Long-Zhang Dong,<sup>[a]</sup> Shun-Li Li,<sup>[a]</sup> Yu-He Kan,<sup>\*,[b]</sup> and Ya-Qian Lan<sup>\*,[a]</sup>

**Abstract:** The energy crisis and environmental pollution have forced scientists to explore alternative energy conversion and storage devices. The anodic reactions of these devices are all oxygen evolution reactions (OER), so the development of efficient OER electrocatalysts is of great significance. At the same time, understanding the reaction mechanism of OER is conducive to the rational design of efficient OER electrocatalysts. In general, catalytic active centers play a direct role in OER performance. In this paper, a series of stable bimetallic metal–organic frameworks (MOFs, named as Fe<sub>3</sub>-

Co<sub>n</sub>-X<sub>2</sub>, *n* = 2, 3 and X = F, Cl, Br) with similar structure were synthesized by changing the halogen coordinated with the cobalt metal active center, aiming to investigate the influence of halogen substitution effect on OER performance. It was found that the OER activity of Fe<sub>3</sub>-Co<sub>3</sub>-F<sub>2</sub> is much better than Fe<sub>3</sub>-Co<sub>2</sub>-Cl<sub>2</sub> and Fe<sub>3</sub>-Co<sub>2</sub>-Br<sub>2</sub>, indicating that the regulation of the electronegativity change of the coordination halogen atom can regulate the coordination electron structure of the metal active center, thereby achieving effective regulation of OER performance.

## Introduction

Due to the increasing demand for energy and more and more serious environmental pollution,<sup>[1]</sup> scientists urgently need to explore clean and efficient energy conversion and storage devices.<sup>[2]</sup> Nowadays, the usual energy conversion and storage devices are water splitting which can produce clean hydrogen fuel,<sup>[3]</sup> fuel cells which can convert chemical energy into electrical energy<sup>[4]</sup> and metal–air batteries which can be used to store electrical energy.<sup>[5]</sup> What the three have in common is that the anodic reactions are all oxygen evolution reactions (OER).<sup>[6]</sup> Since OER involves the transfer of four electrons<sup>[7]</sup> and the formation of oxygen double bonds,<sup>[8]</sup> it has a high energy barrier and does not easily occur spontaneously.<sup>[9]</sup> Therefore, we need to add an electrocatalyst which is able to lower the energy barrier and increase the reaction rate.<sup>[10]</sup> The electrocatalysts re-

ported so far can be divided into nanostructure electrocatalysts and crystalline molecular electrocatalysts.<sup>[11]</sup> The former are highly active and easy to recycle,<sup>[12]</sup> but lack clear structural information, such as the wide distribution of defects and the complex active components, which poses great challenges to the investigation of the reaction mechanism.<sup>[13]</sup> In contrast, the latter possess conveniently designed structures, which is beneficial to study the mechanism.<sup>[14]</sup> But instability can lead to poor recoverability and limited application.<sup>[15]</sup> Metal–organic frameworks (MOFs) are a class of periodically arranged crystalline porous materials.<sup>[16]</sup> Their well-defined structures can accurately reflect the catalytic active sites, and their structural designability helps to systematically study the influence of specific functional groups or the structural environment on the reaction mechanism.<sup>[17]</sup> For example, a stable MOF structure can be used to study the effects of different metals, ligands and coordination environments during the OER process. However, most MOFs are unstable in water, especially in acidic or alkaline aqueous solutions,<sup>[17b,18]</sup> which greatly limits the development of MOFs in the field of OER. At present, reports of MOFs for OER are still very finite. The reported MOF research scope mainly involves the influences of different mono-metal active sites,<sup>[19]</sup> multi-metal active sites,<sup>[20]</sup> or mixed ligands,<sup>[21]</sup> different functional groups of ligands, and reaction intermediates<sup>[22]</sup> on OER performance and reaction mechanism. But the impact of the coordination environment of catalytic centers on OER performance has not been reported.

Herein, we report a series of stable MOFs whose formulas are [Fe<sub>3</sub>(μ<sub>3</sub>-O)(bdc)<sub>3</sub>][Co<sub>2-3</sub>(trz)<sub>3</sub>F<sub>2</sub>(H<sub>2</sub>O)<sub>3.32</sub>(OH<sup>-</sup>)<sub>0.68</sub>] (named Fe<sub>3</sub>-Co<sub>3</sub>-F<sub>2</sub>, bdc = terephthalic acid, trz = 1,2,4-triazole) and [Fe<sub>3</sub>(μ<sub>3</sub>-O)(bdc)<sub>3</sub>][Co<sub>2</sub>(trz)<sub>3</sub>X<sub>2</sub>(H<sub>2</sub>O)<sub>4</sub>] (named Fe<sub>3</sub>-Co<sub>2</sub>-X<sub>2</sub>, X = Cl, Br). And their structures are similar. By replacing the halogen ions directly coordinated with the metal centers of the dinuclear/tri-

[a] J.-N. Lu, Dr. J. Liu, L.-Z. Dong, Prof. S.-L. Li, Prof. Y.-Q. Lan  
Jiangsu Collaborative Innovation Centre  
of Biomedical Functional Materials  
School of Chemistry and Materials Science  
Nanjing Normal University  
No. 1, Wenyuan Road  
Nanjing 210023 (China)  
E-mail: liuj@njnu.edu.cn  
yqlan@njnu.edu.cn

[b] Prof. Y.-H. Kan  
Jiangsu Province Key Laboratory for  
Chemistry of Low-Dimensional Materials  
School of Chemistry and Chemical Engineering  
Huaiyin Normal University  
Huai'an 223300 (P.R. China)  
E-mail: yhkan.cn@gmail.com

Supporting information and the ORCID identification number(s) for the author(s) of this article can be found under:  
<https://doi.org/10.1002/chem.201903482>.



nuclear cobalt clusters in the MOF structure, we systematically studied for the first time the effects of different electronegative coordination atoms on the OER performance. In theory, the order of electronegativity is  $F > Cl > Br$ . The greater the electronegativity, the greater the electron-withdrawing ability, so the electron density of Co coordinated with F is the smallest, which is more conducive to the chemical adsorption of  $OH^-$ ,<sup>[23]</sup> and promotes the OER performance of the Co active center under alkaline conditions. At the same time, the experimental results further validate this rule: at 0.1 M KOH, at a current density of  $10 \text{ mA cm}^{-2}$ , the overpotentials for OER are  $Fe_3-Co_3-F_2 < Fe_3-Co_2-Cl_2 < Fe_3-Co_2-Br_2$ .

## Results and Discussion

We synthesized a series of similar bimetallic MOFs using a simple solvothermal method by replacing the metal source. X-ray crystallographic analysis shows that these three MOFs are composed of classical O-centered trinuclear iron clusters ( $Fe_3$ ) and dinuclear/trinuclear cobalt clusters ( $Co_3-F_2$  and  $Co_2-X_2$ ,  $X = Cl, Br$ ). Then both of clusters act as building units to construct a 3D framework by bdc and trz ligands. In addition, the space group of the three MOFs is  $P6_3/mmc$ . Through topology analysis,  $Fe_3-Co_3-F_2$  is a three-nodal 3,6,9-connected network, while the  $Fe_3-Co_2-Cl_2$  is a two-nodal 3,9-connected network (Figure S1 in Supporting Information). The 3D frameworks of three MOFs are shown in Figure 1. The  $Fe_3$  trinuclear cluster contains

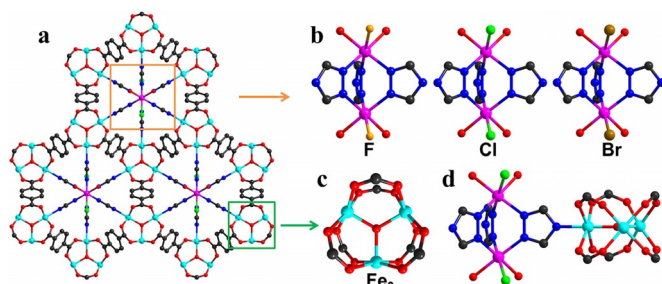


**Figure 1.** 3D framework of a)  $Fe_3-Co_n-X_n$ , b) the cobalt clusters with different halogen atoms, c) the  $Fe_3$  trinuclear cluster, and d) the connection of the  $Fe_3$  trinuclear cluster and the  $Co_2-X_2$  dinuclear cluster. Color code: red, O; blue, N; black, C; light blue, Fe; pink, Co; yellow, F; green, Cl; brown, Br.

three Fe atoms, one  $\mu_3-O$  and six carboxyl groups from bdc ligands (Figure 1c). The  $Co_2-X_2$  dinuclear cluster is a paddle-wheel dimer, consisting of two Co atoms and three trz ligands, and each Co atom coordinates one X ( $X = Cl, Br$ ) ion and two oxygen atoms from two water molecules (Figure 1b).  $Co_3-F_2$  is similar to  $Co_2-X_2$  ( $X = Cl, Br$ ). Since the radius of the F atom is smaller than that of Cl and Br, another Co atom is placed in the middle of the adjacent  $Co_2-F_2$  cluster (Figure S2). And two Co atoms are connected by the oxygen bridge and the fluorine bridge, forming the Co–F chains. Each  $Fe_3$  trinuclear cluster is connected to six  $Fe_3$  trinuclear clusters through bdc ligands (Figure S3). Moreover, every  $Fe_3$  trinuclear cluster connects three  $Co_n-X_2$  dinuclear/trinuclear clusters by trz ligands (Figure 1d, Figure S4 and S5). Then both of the  $Fe_3$  and  $Co_3-F_2$  or

$Co_2-X_2$  clusters act as building blocks to construct a 3D framework.

Under the optical microscope, it is clear to observe that  $Fe_3-Co_3-F_2$  and  $Fe_3-Co_2-Cl_2$  are reddish-brown polyhedron-shaped crystals. However,  $Fe_3-Co_2-Br_2$  is microcrystalline and is too small to see clearly using the optical microscope. So their morphologies were further displayed by scanning electron microscopy (SEM) images (Supporting Information, Figure S8). It is obvious that these three MOFs are uniform crystals with regular shape. As the SEM-EDS elemental mapping images of  $Fe_3-Co_3-F_2$ ,  $Fe_3-Co_2-Cl_2$  and  $Fe_3-Co_2-Br_2$  (Figure 2c, Supporting Infor-

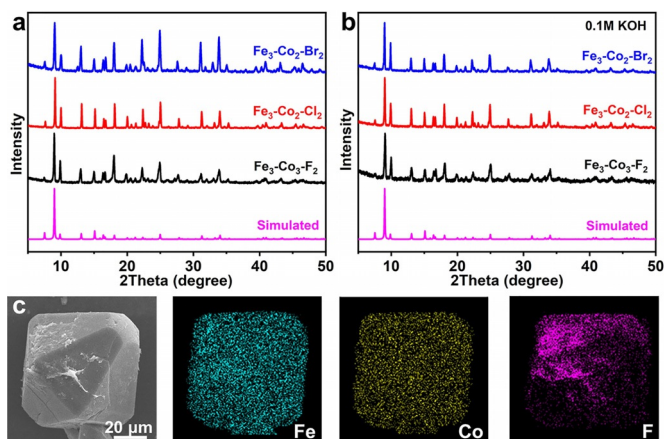


**Figure 2.** PXRD patterns of a)  $Fe_3-Co_n-X_n$ , b)  $Fe_3-Co_n-X_n$  immersed in 0.1 M KOH for 24 h, and c) SEM image and elemental mapping of  $Fe_3-Co_3-F_2$ .

mation Figure S9 and S10) show, the element distribution is highly uniform, which indicates that halogen is evenly incorporated into these MOFs. In addition, the basic composition of these MOFs can be further ascertained by energy-dispersive X-ray spectroscopy (EDS) and X-ray photoelectron spectroscopy (XPS). The EDS spectra (Supporting Information, Figure S11–S13) reveal that  $Fe_3-Co_n-X_n$  consists of Fe, Co, C, N, O and X ( $X =$  the corresponding halogen, F, Cl and Br) without other impurities. And XPS survey spectra of  $Fe_3-Co_3-F_2$ ,  $Fe_3-Co_2-Cl_2$  and  $Fe_3-Co_2-Br_2$  (Supporting Information, Figure S14a) also prove this fact. Besides, according to XPS, the atomic ratio of Fe and Co for  $Fe_3-Co_3-F_2$ ,  $Fe_3-Co_2-Cl_2$  and  $Fe_3-Co_2-Br_2$  are 1.71:1, 1.45:1 and 1.53:1, respectively, which correspond to those calculated by the molecular formulas. Moreover, the results of XPS not only revealed the surface chemical composition, but also established the valence state of metal ions. The XPS  $Fe\ 2p_{3/2}$  peak located at 713.8 eV and  $2p_{1/2}$  peak located at 725.5 eV indicate that Fe has an oxidation state of +3 in the MOF structure (Figure S14f). Further, XPS  $Co\ 2p_{3/2}$  at 782.3 eV and  $2p_{1/2}$  at 797.5 eV shows that Co has an oxidation state of +2 inside the material (Figure S14e).

The structures of  $Fe_3-Co_n-X_n$  were fully characterized by powder X-ray diffraction (PXRD), Fourier transform infrared spectroscopy (FTIR), thermogravimetric analysis (TGA) and  $N_2$  adsorption tests. The PXRD patterns not only exhibit that the structures of as-prepared MOFs are consistent with the simu-



lated pattern from single-crystal X-ray diffraction, but also prove high purity and good crystallinity of these three MOFs (Figure 2a). The FTIR was then performed to disclose the structural features of the three MOFs (Figure S15). In order to check the chemical stability of these MOFs, we immersed 50 mg crystals in 10 mL different pH aqueous solutions (0.1 M KOH and 0.1 M HCl) at room temperature. After 24 hours, the PXRD patterns of  $\text{Fe}_3\text{-Co}_n\text{-X}_2$  remain unchanged in water at pH 1–13 (Figure 2b and Figure S16). This result indicates that these MOFs are stable in a wide pH range from 1 to 13 and have the potential to act as OER electrocatalysts in alkaline condition. Furthermore, TGA was measured to confirm the thermal stability of  $\text{Fe}_3\text{-Co}_n\text{-X}_2$  under  $\text{O}_2$  atmosphere from room temperature to  $800^\circ\text{C}$ , which reveals that  $\text{Fe}_3\text{-Co}_n\text{-X}_2$  could release all guest solvent molecules below about  $200^\circ\text{C}$  whilst maintaining high crystallinity. Additionally,  $\text{Fe}_3\text{-Co}_n\text{-X}_2$  remains stable until  $380^\circ\text{C}$  or so (Supporting Information, Figure S17).

$\text{N}_2$  adsorption-desorption isotherms were measured at 77 K, and show structural porosity. All curves show typical type-I isotherms, which exhibit rapid nitrogen absorption at low relative pressures. As shown in Figures S18–20 in Supporting Information,  $\text{Fe}_3\text{-Co}_3\text{-F}_2$  has a saturation uptake of  $171\text{ cm}^3(\text{STP})\text{g}^{-1}$ , which is larger than  $\text{Fe}_3\text{-Co}_2\text{-Cl}_2$  ( $165\text{ cm}^3(\text{STP})\text{g}^{-1}$ ) and  $\text{Fe}_3\text{-Co}_2\text{-Br}_2$  ( $116\text{ cm}^3(\text{STP})\text{g}^{-1}$ ). Correspondingly, the pore volumes of  $\text{Fe}_3\text{-Co}_2\text{-Cl}_2$  ( $0.254\text{ cm}^3\text{g}^{-1}$ ) and  $\text{Fe}_3\text{-Co}_2\text{-Br}_2$  ( $0.188\text{ cm}^3\text{g}^{-1}$ ) are obviously smaller than  $\text{Fe}_3\text{-Co}_3\text{-F}_2$  ( $0.326\text{ cm}^3\text{g}^{-1}$ ). The three MOFs possess Brunauer–Emmett–Teller (BET) specific surface areas of 477 ( $\text{Fe}_3\text{-Co}_3\text{-F}_2$ ), 474 ( $\text{Fe}_3\text{-Co}_2\text{-Cl}_2$ ) and  $329\text{ m}^2\text{g}^{-1}$  ( $\text{Fe}_3\text{-Co}_2\text{-Br}_2$ ), respectively. The inherent porosity of these MOFs with large surface areas and accessible pores can improve the utilization of catalyst, based on rapid electrolyte permeation/diffusion, expedient adsorption of reactants (water molecules) and free desorption of products (oxygen) during the OER catalytic process. The corresponding pore-size distribution was calculated by Non-Local Density Functional Theory (NLDFT) from the  $\text{N}_2$  adsorption curves. These reveal that the pore size of  $\text{Fe}_3\text{-Co}_n\text{-X}_2$  is about 0.6 nm (Figure S21). Therefore, the microporous characteristic of  $\text{Fe}_3\text{-Co}_n\text{-X}_2$  is demonstrated. Based on the above  $\text{N}_2$  adsorption-desorption data, we can draw a conclusion that  $\text{Fe}_3\text{-Co}_3\text{-F}_2$  possesses a larger pore size compared with others. The enlargement of pore volume for  $\text{Fe}_3\text{-Co}_3\text{-F}_2$  may provide larger accessible surface and more exposure to catalytic active sites and more efficient mass transfer, making it a better electrocatalyst for OER than  $\text{Fe}_3\text{-Co}_2\text{-Cl}_2$  and  $\text{Fe}_3\text{-Co}_2\text{-Br}_2$ .

The electrocatalytic property of  $\text{Fe}_3\text{-Co}_n\text{-X}_2$  for OER under 0.1 M KOH was tested in a typical three-electrode system, where carbon cloth (CC) coated catalysts with a loading of  $1\text{ mg cm}^{-2}$  were used as the working electrode directly. Acetylene black (AB) was introduced to mix with the  $\text{Fe}_3\text{-Co}_n\text{-X}_2$  to improve the conductivity. By measuring the OER activity of different mass ratios of  $\text{Fe}_3\text{-Co}_3\text{-F}_2$  and AB (Supporting Information, Figure S22), we chose and applied the optimal mass ratio (that is the mass ratio of  $\text{Fe}_3\text{-Co}_3\text{-F}_2$  and AB is 2:1) in the following experiments. All the data were acquired without  $iR$ -correction. The polarization curves of as-prepared MOFs were obtained by linear sweep voltammetry (LSV) at a scan rate of

$5\text{ mVs}^{-1}$  (Figure 3a). Apparently,  $\text{Fe}_3\text{-Co}_3\text{-F}_2$  exhibits higher current density and more negative potential than  $\text{Fe}_3\text{-Co}_2\text{-Cl}_2$  and  $\text{Fe}_3\text{-Co}_2\text{-Br}_2$ . We further compared the overpotentials of different catalysts at a current density of  $10\text{ mA cm}^{-2}$  ( $\eta_{10}$ ),<sup>[24]</sup> which

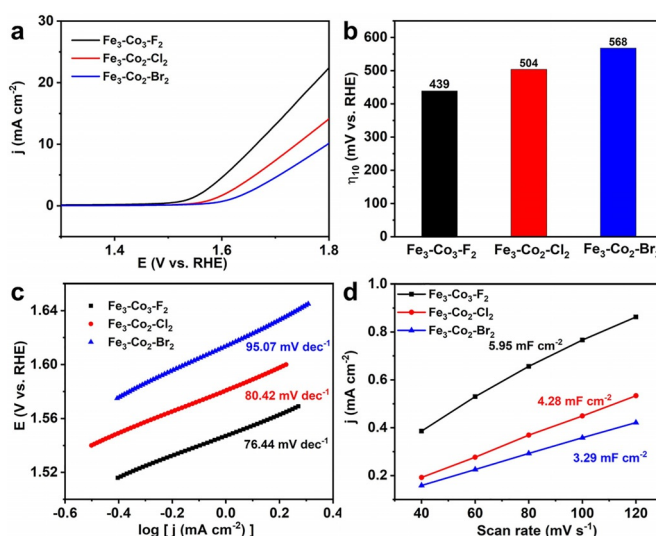


**Figure 3.** a) LSV curves of  $\text{Fe}_3\text{-Co}_n\text{-X}_2$  for OER in 0.1 M KOH. b) A comparison of the overpotential at current density of  $10\text{ mA cm}^{-2}$ . c) Corresponding Tafel plots of  $\text{Fe}_3\text{-Co}_n\text{-X}_2$  for OER in 0.1 M KOH. d) Plots used for evaluating the  $C_{dl}$  of  $\text{Fe}_3\text{-Co}_n\text{-X}_2$ .

represents the current density of a realistic device with 12.3 % solar-hydrogen efficiency.<sup>[25]</sup> As a result, the potential of  $\text{Fe}_3\text{-Co}_3\text{-F}_2$  is 1.669 V versus RHE (reversible hydrogen electrode) at a current density of  $10\text{ mA cm}^{-2}$ , corresponding to an overpotential of 439 mV. According to Figure 3b, the overpotentials of  $\text{Fe}_3\text{-Co}_2\text{-Cl}_2$  and  $\text{Fe}_3\text{-Co}_2\text{-Br}_2$  are 504 and 568 mV, respectively. In comparison with the other two,  $\text{Fe}_3\text{-Co}_3\text{-F}_2$  shows the smallest overpotential and the most remarkable OER performance. Besides, the kinetics of catalytic oxygen evolution were analyzed using the Tafel plots, which were calculated based on LSVs. By plotting  $\log(j)$  versus overpotential and fitting the linear portion of the curves, Figure 3c demonstrates that  $\text{Fe}_3\text{-Co}_3\text{-F}_2$  has smaller Tafel slope ( $76.44\text{ mV dec}^{-1}$ ) than  $\text{Fe}_3\text{-Co}_2\text{-Cl}_2$  ( $80.42\text{ mV dec}^{-1}$ ) and  $\text{Fe}_3\text{-Co}_2\text{-Br}_2$  ( $95.07\text{ mV dec}^{-1}$ ), indicating faster charge transport and more favorable reaction kinetics after regulating MOFs through halogen substitution. As a consequence, the high activity of  $\text{Fe}_3\text{-Co}_3\text{-F}_2$  toward OER is confirmed by the both of small overpotential and low Tafel slope.

Specifically, the turnover frequency (TOF) is one of the common parameters to assess the OER performance. The TOF and potential curves of the  $\text{Fe}_3\text{-Co}_n\text{-X}_2$  are shown in Figure S23. As Figure S23b shows, at the overpotential of 400 mV, the TOF value of  $\text{Fe}_3\text{-Co}_3\text{-F}_2$  ( $0.0102\text{ s}^{-1}$ ) is superior to that of  $\text{Fe}_3\text{-Co}_2\text{-Cl}_2$  ( $0.0046\text{ s}^{-1}$ ) and  $\text{Fe}_3\text{-Co}_2\text{-Br}_2$  ( $0.0023\text{ s}^{-1}$ ). This phenomenon suggests that  $\text{Fe}_3\text{-Co}_3\text{-F}_2$  performs as a better catalytic in OER.

For practical application, it is essential to ensure the long-term durability of electrocatalysts.<sup>[26]</sup> As shown in the Supporting Information, Figures S24–S26, the long-term operation stability was evaluated by chronopotentiometric curves at



10 mA cm<sup>-2</sup>. The *i*-*t* curves of Fe<sub>3</sub>-Co<sub>n</sub>-X<sub>2</sub> show a slight reduction of current density after a long period of test (18 h), proving the superior stability of these MOFs in OER process. Moreover, there is almost no difference between all LSV curves before and after 2000 cyclic voltammetry (CV) cycles (Figure S27). Both results indicate that Fe<sub>3</sub>-Co<sub>n</sub>-X<sub>2</sub> remains stable during the prolonged OER testing. Besides, the carbon cloth coated catalyst (1 mg) was directly used to measure PXRD before and after OER testing (Figure S28). Although the intensity of peaks is low because of the small loading amounts, all peaks are in good agreement with the simulation, except for several peaks belong to C (JCPDS NO. 3-401). This proves again that three MOFs retain their structure and crystallinity after the OER measurements. And after OER, we tested inductively coupled plasma atomic emission spectroscopy (ICP-AES) of the electrolyte. The result is that only about 2% catalysts dissolve into the electrolyte, fully demonstrating the stability of the catalyst.

In order to understand the reasons for the different catalytic activity of Fe<sub>3</sub>-Co<sub>n</sub>-X<sub>2</sub>, the possible factors that were likely to influence activity were studied carefully. As a kind of porous material, MOFs have a uniform distribution of possible active centers through the entire material and high accessibility as a result of open channels. So MOFs have higher specific surface area and more exposed active sites. Therefore, we measured the cyclic voltammetry to calculate the electrochemical double layer capacitance (*C*<sub>dl</sub>) and further evaluate the electrochemically-active surface area (ECSA). CV curves of Fe<sub>3</sub>-Co<sub>n</sub>-X<sub>2</sub> were performed under the potential range of 1.198–1.298 V versus RHE with different scan rates from 40 to 120 mV s<sup>-1</sup>. The slopes of the curves represent *C*<sub>dl</sub> in Figure 3 d and Figures S29–S31. After replacing chlorine and bromine with fluorine, the *C*<sub>dl</sub> of Fe<sub>3</sub>-Co<sub>3</sub>-F<sub>2</sub> (5.95 mF cm<sup>-2</sup>) is meaningfully improved, again emphasizing the high activity of the modified materials and indicating more exposure of metal active sites in Fe<sub>3</sub>-Co<sub>3</sub>-F<sub>2</sub>. Since the *C*<sub>dl</sub> is proportional to the ECSA, this conclusion reflects that Fe<sub>3</sub>-Co<sub>3</sub>-F<sub>2</sub> has the largest ECSA among these three OER electrocatalysts in alkaline electrolyte. Therefore, more exposure and enhanced utilization of electroactive sites on the larger active surface of Fe<sub>3</sub>-Co<sub>3</sub>-F<sub>2</sub> greatly promotes its high OER activity.

With the purpose of investigating charge transport kinetics and Nyquist plots, the electrochemical impedance spectroscopy (EIS) of Fe<sub>3</sub>-Co<sub>n</sub>-X<sub>2</sub> were measured at the potential of 1.614 V versus RHE. As seen from Figure S32, the diameter of semicircles is in line with the charge transfer resistance (*R*<sub>ct</sub>) in the Nyquist plot. Moreover, the charge transfer resistance (*R*<sub>ct</sub>) changes greatly after halogen substitution. From the results of EIS, the *R*<sub>ct</sub> value of Fe<sub>3</sub>-Co<sub>2</sub>-Cl<sub>2</sub> (14.63 Ω) and Fe<sub>3</sub>-Co<sub>2</sub>-Br<sub>2</sub> (23.46 Ω) clearly exceeded that of Fe<sub>3</sub>-Co<sub>3</sub>-F<sub>2</sub> (5.687 Ω), confirming that Fe<sub>3</sub>-Co<sub>3</sub>-F<sub>2</sub> has the lowest mass transfer resistance and the fastest charge transfer rate during OER.

It is commonly believed that the synergistic effect<sup>[27]</sup> of the bimetal can effectively promote the catalytic performance of OER by modifying the electronic structure of the metal active center. Apart from this, changing the coordination environment of metal active center will also modify its electronic

structure, leading to an effect on their OER performance. In Fe<sub>3</sub>-Co<sub>n</sub>-X<sub>2</sub>, only the Co atoms of the Co<sub>n</sub>-X<sub>2</sub> cluster have unsaturated coordination. Therefore, the Co atoms can act as catalytic active sites for binding and oxidizing water molecules. In this work, we adjusted the coordination structure of cobalt by replacing the halogen atom directly coordinated with cobalt, thereby regulating the electronic structure of cobalt. In theory, halogen anions are electron withdrawing groups and the greater the electronegativity, the stronger the electron absorption capability. Therefore, based on the order of electronegativity (F > Cl > Br), fluoride ions have the largest electron-withdrawing ability, resulting in the lowest electron density of Co atoms in Fe<sub>3</sub>-Co<sub>3</sub>-F<sub>2</sub>. Experimentally, the electronic properties of Fe<sub>3</sub>-Co<sub>n</sub>-X<sub>2</sub> were reflected by XPS. As shown in Figure 4a, the

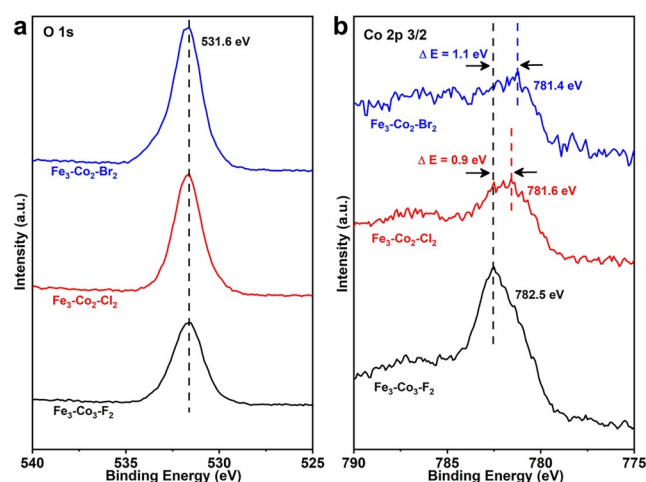


**Figure 4.** a) O1s spectra and b) Co2p<sub>3/2</sub> spectra of Fe<sub>3</sub>-Co<sub>3</sub>-F<sub>2</sub>, Fe<sub>3</sub>-Co<sub>2</sub>-Cl<sub>2</sub>, and Fe<sub>3</sub>-Co<sub>2</sub>-Br<sub>2</sub>.

binding energy of O 1s in the three MOFs is same as each other, corresponding to the species of O=C–O (531.6 eV). From XPS Co 2p<sub>3/2</sub> spectra (Figure 4b), compared to Fe<sub>3</sub>-Co<sub>2</sub>-Cl<sub>2</sub> (781.6 eV) and Fe<sub>3</sub>-Co<sub>2</sub>-Br<sub>2</sub> (781.4 eV), the binding energy of Co 2p<sub>3/2</sub> in Fe<sub>3</sub>-Co<sub>3</sub>-F<sub>2</sub> shifted to high binding energy (782.5 eV), indicating a modified local electronic structure of Co and suggesting less electrons are accepted, in line with the theory prediction. After that, we further studied the structure–activity relationship of these MOFs. The shift to higher binding energy may be attributed to the changes in the coordination environment of the activity centers caused by replacing Cl and Br with F, and it is crucial to regulate the electronic properties of the active centers, thus promoting OER catalysis. As is known to all, the effective adsorption of hydroxide and water molecules on the catalyst surface plays a key role in the OER process. When the electron density of the Co atom is impaired, it can make the catalytic active site (Co) more electrophilic, thereby promoting the adsorption and reaction of the OH group with Fe<sub>3</sub>-Co<sub>3</sub>-F<sub>2</sub>, leading to the enhancement of OER activity in alkaline solution. Based on our experimental results, in addition to the tailoring of MOFs electronic properties demonstrated by XPS, the halogen replacement can improve ECSA and thus enhance the OER activity.



## Conclusion

In summary, a series of MOFs have been synthesized by introducing mixed metal and organic linker through a mild solvothermal method. The resulting MOFs were fully characterized by X-ray crystallographic analysis, PXRD, FTIR, SEM, EDS, mapping and XPS, showing they have similar host structures and morphology. Engineering the electronic structure of metal active sites in MOFs by halogen coordination substitution can improve their electrocatalytic OER performance. Among these similar MOFs,  $\text{Fe}_3\text{-Co}_3\text{-F}_2$  can serve as an efficient electrocatalyst for OER with a low overpotential of 439 mV at  $10 \text{ mA cm}^{-2}$  and a Tafel slope of  $76.44 \text{ mV dec}^{-1}$ . More importantly, this impressive catalytic activity is attributed to the improved intrinsic activity of the catalytic center by adjusting electronic structure using F with high electronegativity. This will provide a new strategy of engineering efficient MOF-based electrocatalysts for OER application.

## Experimental Section

### Preparation of $\text{Fe}_3\text{-Co}_3\text{-F}_2$

$\text{Fe}(\text{NO}_3)_3 \cdot 9\text{H}_2\text{O}$  (364 mg),  $\text{Co}(\text{NO}_3)_2 \cdot 6\text{H}_2\text{O}$  (175 mg), terephthalic acid (bdc, 150 mg) and 1,2,4-triazole (trz, 65 mg) were dissolved in 3.2 mL DMF by ultrasonication, followed by mixing with hydrofluoric acid (HF, 40%, 0.11 mL). Subsequently, the mixture solution was transferred into a 15 mL Teflon-lined stainless-steel autoclave, sealed and maintained at  $150^\circ\text{C}$  for 24 h. After cooling down to room temperature, the resultant crystals were collected by filtration and washed with DMF.

### Preparation of $\text{Fe}_3\text{-Co}_2\text{-Cl}_2$

$\text{FeCl}_3 \cdot 6\text{H}_2\text{O}$  (243 mg),  $\text{CoCl}_2 \cdot 6\text{H}_2\text{O}$  (143 mg), bdc (150 mg) and trz (65 mg) were dissolved in 3.2 mL DMF by ultrasonication, followed by mixing with hydrofluoric acid (HF, 40%, 0.13 mL). Subsequently, the mixture solution was transferred into a 15 mL Teflon-lined stainless-steel autoclave, sealed and maintained at  $150^\circ\text{C}$  for 24 h. After cooling down to room temperature, the resultant crystals were collected by filtration and washed with DMF.

### Preparation of $\text{Fe}_3\text{-Co}_2\text{-Br}_2$

$\text{FeBr}_3$  (266 mg),  $\text{CoBr}_2 \cdot x\text{H}_2\text{O}$  (131 mg), bdc (150 mg) and trz (65 mg) were dissolved in 3.2 mL DMF by ultrasonication, followed by mixing with trifluoroacetic acid (TFA, 0.19 mL). Subsequently, the mixture solution was transferred into a 15 mL Teflon-lined stainless-steel autoclave, sealed and maintained at  $150^\circ\text{C}$  for 24 h. After cooling down to room temperature, the resultant crystals were collected by filtration and washed with DMF.

### Characterization

Powder X-ray diffraction (PXRD) patterns were recorded on a Rigaku D/Max 2500/PC diffractometer equipped with graphite monochromatized  $\text{Cu}_{\text{K}\alpha}$  radiation ( $\lambda = 1.54060 \text{ \AA}$ ) at 40 kV and 100 mA. Fourier transform infrared spectroscopy (FTIR) was measured on a NEXUS670 using KBr pellets, in the range of  $4000\text{--}400 \text{ cm}^{-1}$ . Thermogravimetric analyses (TGA) were carried out on a PerkinElmer Diamond DSC Pyris analyzer under oxygen, with a heating rate of  $10^\circ\text{C min}^{-1}$  from room temperature to  $800^\circ\text{C}$ .  $\text{N}_2$

adsorption-desorption isotherms were determined by using a Quantachrome Instruments Autosorb IQ2 at 77 K. Before the measurement, the catalysts were degassed at  $120^\circ\text{C}$  for 12 h. The pore size distributions were measured by the Non-Local Density Functional Theory (NLDFT) method. Scanning electron microscopy (SEM) and energy-dispersive X-ray spectroscopy (EDS) of MOFs was analyzed by SEM (JEOL JSM-7600F) with acceleration voltage of 10 kV and 15 kV, respectively. MOFs content in the electrolyte is calculated by metal content, which was obtained by inductively coupled plasma atomic emission spectroscopy (ICP-AES) using an Induction Coupled Plasma Quantometer (Jarrell-Ash 1100 + 2000). X-ray photoelectron spectroscopy (XPS) were recorded using an Escalab 250Xi instrument from Thermo Scientific equipped with an  $\text{Al}_{\text{K}\alpha}$  microfocused X-ray source and using the C 1s peak at 284.6 eV as an internal standard.

### Single-crystal X-ray analyses

The diffraction data of  $\text{Fe}_3\text{-Co}_3\text{-F}_2$  and  $\text{Fe}_3\text{-Co}_2\text{-Cl}_2$  were collected on Bruker AXS Apex II CCD diffractometer ( $\text{Mo}_{\text{K}\alpha}$ ,  $\lambda = 0.71069 \text{ \AA}$ ) at 293 K. All non-hydrogen atoms were refined with anisotropic displacement parameters and hydrogen positions were fixed at calculated positions and refined isotropically. All structures were solved by direct methods and refined with the full-matrix least-squares technique on  $F^2$  by the SHELX-2014<sup>[28]</sup> program package and Olex2<sup>[29]</sup> software. All the solvent molecules, which are highly disordered and not able to be modeled, were treated by the SQUEEZE<sup>[30]</sup> routine in PLATON.<sup>[31]</sup> The topological analyses were performed with TOPOS.<sup>[32]</sup> The detailed structure determination parameters and crystallographic data are shown in Table S1. CCDC 1943179 ( $\text{Fe}_3\text{-Co}_2\text{-Cl}_2$ ) and 1943180 ( $\text{Fe}_3\text{-Co}_3\text{-F}_2$ ) contain the supplementary crystallographic data for this paper. These data are provided free of charge by The Cambridge Crystallographic Data Centre.

### Electrochemical measurements

Electrochemical measurements were carried out in a three-electrode cell with carbon cloth (CC,  $2 \times 1 \text{ cm}$ ) as working electrode, carbon rod as the counter electrode and a Ag/AgCl (KCl saturated) electrode as the reference electrode, controlled by the electrochemical workstation (CHI 660e) at ambient conditions. Prior to the measurements, a flow of  $\text{N}_2$  was bubbled for at least 30 minutes to remove the dissolved oxygen in the electrolyte. The measured potentials versus the reversible hydrogen electrode (RHE) were converted according to the equation:  $E (\text{V vs. RHE}) = E (\text{V vs. Ag/AgCl}) + 0.197 + 0.059 \times \text{pH}$ .

For preparation of the working electrode, 15 mg catalyst were ground to powder and then mixed with acetylene black (AB, 7.5 mg) uniformly. 15 mg of the uniform mixture was dispersed in 1 mL of solvent (750  $\mu\text{L}$   $\text{H}_2\text{O}$ , 210  $\mu\text{L}$  EtOH and 40  $\mu\text{L}$  Nafion) by ultrasonication to form a homogeneous ink. Subsequently, 100  $\mu\text{L}$  of the ink was covered onto the both sides of the carbon cloth and dried at room temperature for measurements. Prior to modification, the carbon cloth ( $2 \times 1 \text{ cm}$ ) was pretreated with ethanol, acetone and nitric acid. In addition, the area of coated catalyst was controlled to  $1 \times 1 \text{ cm}$ . In all measurements, the loading mass of the catalysts on the carbon cloth was  $1 \text{ mg cm}^{-2}$ , and the mass ratio of the as-synthesized crystals and AB was 2:1, unless otherwise specified.

The linear scan voltammetry (LSV) was performed at a scan rate of  $5 \text{ mV s}^{-1}$ . The cyclic voltammogram (CV) was recorded with a scan rate of  $100 \text{ mV s}^{-1}$ . To estimate the electrochemical active surface area (ECSA) of the catalyst, CV was tested by measuring double-



layer capacitance ( $C_{dl}$ ) under the potential window of 1.198–1.298 V versus RHE with various scan rates of 40–120 mV s<sup>-1</sup>. The electrochemical impedance spectroscopy (EIS) measurement was carried out at 1.614 V versus RHE over a frequency range from 0.1 Hz to 1000 KHz; a 10 mV amplitude of sinusoidal potential perturbation was employed in the measurements. The chronoamperometry was measured at the overpotential corresponding to the current density of 10 mA cm<sup>-2</sup>. All electrochemical measurements were measured without *iR*-correction.

## Turnover frequency calculation

Turnover frequency (TOF) values of catalysts are calculated according to the following equation:  $TOF = (j \times A) / (4 \times F \times m)$ , where  $j$  (A cm<sup>-2</sup>) is the current density during the LSV measurement in 0.1 M KOH,  $A$  is the surface area of the carbon cloth (CC, 1 cm<sup>2</sup>), the number 4 means a four-electron transfer during the formation of per mol O<sub>2</sub>,  $F$  is the Faraday constant (96485 C mol<sup>-1</sup>),  $m$  is the moles of active sites on the electrode (based on all metal).

## Acknowledgements

This work was financially supported by NSFC (No. 21622104, 21701085, 21871141 and 21871142); the NSF of Jiangsu Province of China (No. BK20171032); the Natural Science Research of Jiangsu Higher Education Institutions of China (No. 17KJB150025); Priority Academic Program Development of Jiangsu Higher Education Institutions and the Foundation of Jiangsu Collaborative Innovation Center of Biomedical Functional Materials.

## Conflict of interest

The authors declare no conflict of interest.

**Keywords:** electrocatalysts • electronic structures • halogens • metal–organic frameworks • oxygen evolution reaction

- [1] a) Z. W. Seh, J. Kibsgaard, C. F. Dickens, I. B. Chorkendorff, J. K. Nørskov, T. F. Jaramillo, *Science* **2017**, 355, eaad4998; b) T. R. Cook, D. K. Dogutan, S. Y. Reece, Y. Surendranath, T. S. Teets, D. G. Nocera, *Chem. Rev.* **2010**, 110, 6474–6502; c) Y. Zhou, X. Guan, H. Zhou, K. Ramadoss, S. Adam, H. Liu, S. Lee, J. Shi, M. Tsuchiya, D. D. Fong, S. Ramanathan, *Nature* **2016**, 534, 231–234.
- [2] J. Suntivich, H. A. Gasteiger, N. Yabuuchi, H. Nakanishi, J. B. Goodenough, Y. Shao-Horn, *Nat. Chem.* **2011**, 3, 546–550.
- [3] a) J. Jian, Y. X. Xu, X. K. Yang, W. Liu, M. S. Fu, H. W. Yu, F. Xu, F. Feng, L. C. Jia, D. Friedrich, R. van de Krol, H. Q. Wang, *Nat. Commun.* **2019**, 10, 2609; b) S. Sultan, J. N. Tiwari, A. N. Singh, S. Zhumagali, M. Ha, C. W. Myung, P. Thangavel, K. S. Kim, *Adv. Energy Mater.* **2019**, 9, 1900624; c) G. Zhang, G. C. Wang, Y. Liu, H. J. Liu, J. H. Qu, J. H. Li, *J. Am. Chem. Soc.* **2016**, 138, 14686–14693.
- [4] a) C. C. Duan, R. J. Kee, H. Y. Zhu, C. Karakaya, Y. C. Chen, S. Ricote, A. Jarry, E. J. Crumlin, D. Hook, R. Braun, N. P. Sullivan, R. O'Hayre, *Nature* **2018**, 557, 217–222; b) X. X. Wang, D. A. Cullen, Y. T. Pan, S. Hwang, M. Y. Wang, Z. X. Feng, J. Y. Wang, M. H. Engelhard, H. G. Zhang, Y. H. He, Y. Y. Shao, D. Su, K. L. More, J. S. Spendelow, G. Wu, *Adv. Mater.* **2018**, 30, 1706758; c) N. Senthilkumar, G. G. Kumar, A. Manthiram, *Adv. Energy Mater.* **2018**, 8, 1702207.
- [5] a) M. D. Zhang, Q. B. Dai, H. G. Zheng, M. D. Chen, L. M. Dai, *Adv. Mater.* **2018**, 30, 1705431; b) J. Pan, Y. Y. Xu, H. Yang, Z. H. Dong, H. F. Liu, B. Y. Xia, *Adv. Sci.* **2018**, 5, 1700691; c) F. Meng, H. Zhong, D. Bao, J. Yan, X. Zhang, *J. Am. Chem. Soc.* **2016**, 138, 10226–10231.
- [6] a) N.-T. Suen, S.-F. Hung, Q. Quan, N. Zhang, Y.-J. Xu, H. M. Chen, *Chem. Soc. Rev.* **2017**, 46, 337–365; b) B. Y. Xia, Y. Yan, N. Li, H. B. Wu, X. W. Lou, X. Wang, *Nat. Energy* **2016**, 1, 15006.
- [7] F. Sun, G. Wang, Y. Ding, C. Wang, B. Yuan, Y. Lin, *Adv. Energy Mater.* **2018**, 8, 1800584.
- [8] X. F. Lu, L. F. Gu, J. W. Wang, J. X. Wu, P. Q. Liao, G. R. Li, *Adv. Mater.* **2017**, 29, 1604437.
- [9] a) Q. S. Yin, J. M. Tan, C. Besson, Y. V. Geletii, D. G. Musaev, A. E. Kuznetsov, Z. Luo, K. I. Hardcastle, C. L. Hill, *Science* **2010**, 328, 342–345; b) X. Zheng, B. Zhang, P. De Luna, Y. Liang, R. Comin, O. Voznyy, L. Han, F. P. G. de Arquer, M. Liu, C. T. Dinh, T. Regier, J. J. Dynes, S. He, H. L. Xin, H. Peng, D. Prendergast, X. Du, E. H. Sargent, *Nat. Chem.* **2018**, 10, 149–154; c) B. Zhang, X. L. Zheng, O. Voznyy, R. Comin, M. Bajdich, M. Garcia-Melchor, L. L. Han, J. X. Xu, M. Liu, L. R. Zheng, F. P. G. de Arquer, C. T. Dinh, F. J. Fan, M. J. Yuan, E. Yassitepe, N. Chen, T. Regier, P. F. Liu, Y. H. Li, P. De Luna, A. Janmohamed, H. L. L. Xin, H. G. Yang, A. Vojvodic, E. H. Sargent, *Science* **2016**, 352, 333–337.
- [10] Y. Q. Zhang, B. Ouyang, J. Xu, G. C. Jia, S. Chen, R. S. Rawat, H. J. Fan, *Angew. Chem. Int. Ed.* **2016**, 55, 8670–8674; *Angew. Chem.* **2016**, 128, 8812–8816.
- [11] J. Q. Shen, P. Q. Liao, D. D. Zhou, C. T. He, J. X. Wu, W. X. Zhang, J. P. Zhang, X. M. Chen, *J. Am. Chem. Soc.* **2017**, 139, 1778–1781.
- [12] B. Y. Guan, X. Y. Yu, H. B. Wu, X. W. Lou, *Adv. Mater.* **2017**, 29, 1703614.
- [13] a) H. Jin, C. Guo, X. Liu, J. Liu, A. Vasileff, Y. Jiao, Y. Zheng, S.-Z. Qiao, *Chem. Rev.* **2018**, 118, 6337–6408; b) T. Ling, D.-Y. Yan, Y. Jiao, H. Wang, Y. Zheng, X. Zheng, J. Mao, X.-W. Du, Z. Hu, M. Jaroniec, S.-Z. Qiao, *Nat. Commun.* **2016**, 7, 12876; c) S. Ji, Y. Chen, Q. Fu, Y. Chen, J. Dong, W. Chen, Z. Li, Y. Wang, L. Gu, W. He, C. Chen, Q. Peng, Y. Huang, X. Duan, D. Wang, C. Draxl, Y. Li, *J. Am. Chem. Soc.* **2017**, 139, 9795–9798.
- [14] a) T. Ghosh, G. Maayan, *Angew. Chem. Int. Ed.* **2019**, 58, 2785–2790; *Angew. Chem.* **2019**, 131, 2811–2816; b) R.-J. Xiang, H.-Y. Wang, Z.-J. Xin, C.-B. Li, Y.-X. Lu, X.-W. Gao, H.-M. Sun, R. Cao, *Chem. Eur. J.* **2016**, 22, 1602–1607.
- [15] a) S. Zhao, Y. Wang, J. Dong, C.-T. He, H. Yin, P. An, K. Zhao, X. Zhang, C. Gao, L. Zhang, J. Lv, J. Wang, J. Zhang, A. M. Khattak, N. A. Khan, Z. Wei, J. Zhang, S. Liu, H. Zhao, Z. Tang, *Nat. Energy* **2016**, 1, 16184; b) S. W. Sheehan, J. M. Thomsen, U. Hintermair, R. H. Crabtree, G. W. Brudvig, C. A. Schmuttenmaer, *Nat. Commun.* **2015**, 6, 6469; c) J. Wang, L. Y. Gan, W. Y. Zhang, Y. C. Peng, H. Yu, Q. Y. Yan, X. H. Xia, X. Wang, *Sci. Adv.* **2018**, 4, eaap7970.
- [16] a) H. Furukawa, K. E. Cordova, M. O'Keeffe, O. M. Yaghi, *Science* **2013**, 341, 1230444; b) H.-C. J. Zhou, S. Kitagawa, *Chem. Soc. Rev.* **2014**, 43, 5415–5418; c) E. M. Miner, T. Fukushima, D. Sheberla, L. Sun, Y. Surendranath, M. Dincă, *Nat. Commun.* **2016**, 7, 10942; d) J. Duan, S. Chen, C. Zhao, *Nat. Commun.* **2017**, 8, 15341; e) L. E. Kreno, K. Leong, O. K. Farha, M. Allendorf, R. P. Van Duyne, J. T. Hupp, *Chem. Rev.* **2012**, 112, 1105–1125.
- [17] a) L. Jiao, Y. Wang, H.-L. Jiang, Q. Xu, *Adv. Mater.* **2018**, 30, 1703663; b) J.-P. Zhang, Y.-B. Zhang, J.-B. Lin, X.-M. Chen, *Chem. Rev.* **2012**, 112, 1001–1033.
- [18] D.-Y. Du, J.-S. Qin, S.-L. Li, Z.-M. Su, Y.-Q. Lan, *Chem. Soc. Rev.* **2014**, 43, 4615–4632.
- [19] P. Manna, J. Debgupta, S. Bose, S. K. Das, *Angew. Chem. Int. Ed.* **2016**, 55, 2425–2430; *Angew. Chem.* **2016**, 128, 2471–2476.
- [20] a) X. L. Wang, L. Z. Dong, M. Qiao, Y. J. Tang, J. Liu, Y. F. Li, S. L. Li, J. X. Su, Y. Q. Lan, *Angew. Chem. Int. Ed.* **2018**, 57, 9660–9664; *Angew. Chem.* **2018**, 130, 9808–9812; b) F. L. Li, Q. Shao, X. Q. Huang, J. P. Lang, *Angew. Chem. Int. Ed.* **2018**, 57, 1888–1892; *Angew. Chem.* **2018**, 130, 1906–1910.
- [21] Z. Q. Xue, Y. L. Li, Y. W. Zhang, W. Geng, B. M. Jia, J. Tang, S. X. Bao, H. P. Wang, Y. A. Fan, Z. W. Wei, Z. S. Zhang, Z. F. Ke, G. Q. Li, C. Y. Su, *Adv. Energy Mater.* **2018**, 8, 1801564.
- [22] a) J. Huang, Y. Li, R. K. Huang, C. T. He, L. Gong, Q. Hu, L. Wang, Y. T. Xu, X. Y. Tian, S. Y. Liu, Z. M. Ye, F. Wang, D. D. Zhou, W. X. Zhang, J. P. Zhang, *Angew. Chem. Int. Ed.* **2018**, 57, 4632–4636; *Angew. Chem.* **2018**, 130, 4722–4726; b) X. F. Lu, P. Q. Liao, J. W. Wang, J. X. Wu, X. W. Chen, C. T. He, J. P. Zhang, G. R. Li, X. M. Chen, *J. Am. Chem. Soc.* **2016**, 138, 8336–8339.



- [23] T. Y. Ma, S. Dai, M. Jaroniec, S. Z. Qiao, *J. Am. Chem. Soc.* **2014**, *136*, 13925–13931.
- [24] S. Zhao, R. Jin, H. Abroshan, C. Zeng, H. Zhang, S. D. House, E. Gottlieb, H. J. Kim, J. C. Yang, R. Jin, *J. Am. Chem. Soc.* **2017**, *139*, 1077–1080.
- [25] J. S. Luo, J. H. Im, M. T. Mayer, M. Schreier, M. K. Nazeeruddin, N. G. Park, S. D. Tilley, H. J. Fan, M. Gratzel, *Science* **2014**, *345*, 1593–1596.
- [26] L. Han, S. Dong, E. Wang, *Adv. Mater.* **2016**, *28*, 9266–9291.
- [27] a) F. L. Li, P. Wang, X. Huang, D. J. Young, H. F. Wang, P. Braunstein, J. P. Lang, *Angew. Chem. Int. Ed.* **2019**, *58*, 7051–7056; *Angew. Chem.* **2019**, *131*, 7125–7130; b) B. Wurster, D. Grumelli, D. Hotger, R. Gutzler, K. Kern, *J. Am. Chem. Soc.* **2016**, *138*, 3623–3626.
- [28] D. Leggas, O. V. Tsodikov, *Acta Crystallogr. Sect. A* **2015**, *71*, 319–324.
- [29] O. V. Dolomanov, L. J. Bourhis, R. J. Gildea, J. A. K. Howard, H. Puschman, *J. Appl. Crystallogr.* **2009**, *42*, 339–341.
- [30] A. Spek, *Acta Crystallogr. Sect. C* **2015**, *71*, 9–18.
- [31] A. Spek, *Acta Crystallogr. Sect. D* **2009**, *65*, 148–155.
- [32] E. V. Alexandrov, V. A. Blatov, A. V. Kochetkov, D. M. Proserpio, *CrystEngComm* **2011**, *13*, 3947–3958.

---

Manuscript received: July 30, 2019

Accepted manuscript online: September 25, 2019

Version of record online: November 15, 2019

---